

Water flipping and the oxygen evolution reaction on Fe₂O₃ nanolayers

Received: 13 June 2024

Accepted: 2 April 2025

Published online: 15 April 2025

 Check for updatesRaïden Speelman¹, Ezra J. Marker¹, Mavis D. Boamah², Jacob Kupferberg³, Justin Z. Bye¹, Mark Engelhard², Yatong Zhao², Alex B. F. Martinson³, Kevin M. Rosso² & Franz M. Geiger¹✉

Hematite photoanodes are promising for the oxygen evolution reaction, however, their high overpotential (0.5–0.6 V) for water oxidation and limited photocurrent make them economically unviable at present. The work needed to orient dipoles at an electrode surface may be an overlooked contribution to the overpotential, especially regarding dipoles of water, the electron source in the oxygen evolution reaction (OER). Here, we employ second harmonic amplitude and phase measurements to quantify the number of net-aligned Stern layer water molecules and the work associated with water flipping, on hematite, an earth abundant OER semiconductor associated with a high overpotential. At zero applied bias, the pH-dependent potentials for Stern layer water molecule flipping exhibit Nernstian behavior. At positive applied potentials and pH 13, approximately one to two monolayers of water molecules points the oxygen atoms towards the electrode, favorable for the OER. The work associated with water flipping matches the cohesive energy of liquid water (44 kJ mol⁻¹) and the OER current density is highest. This current is negligible at pH 5, where the work approaches 100 kJ mol⁻¹. Our findings suggest a causal relationship between the need for Stern layer water flipping and the OER overpotential, which may lead to developing strategies for decreasing the latter.

Strategies to improve hematite photoanode performance include accelerating water oxidation kinetics with catalytic surface coatings¹, slowing down electron–hole recombination², chemical and structural modifications to hematite^{3,4}, including edge-to-face anisotropy⁵, and non-covalent interactions via electrolyte tuning⁶, all of which involve processes occurring at the electrolyte:electrode interface. One important knowledge gap that remains to be bridged is a detailed molecular understanding of the water structure and the electrostatics at hematite:electrolyte interfaces under bias and/or photoexcitation. For example, the work to orient water dipoles in the Stern layer at the interface under applied potential bias may be an overlooked contribution to the overpotential. This work, we posit, is necessary to properly align water's oxygen atom with an oxo group of the

electrode's active site prior to electron transfer. Testing this hypothesis is especially important for pH conditions above the point of zero charge (e.g. pH 13, the commonly employed pH for the OER on hematite)^{7–9}, where, at zero V bias applied, the Stern layer water molecules point their protons towards the negatively charged surface, blocking line-of-sight access of water's oxygen to the active sites that eventually form at positive bias. Obtaining this work requires the quantification of two properties: the number of net-aligned Stern layer water molecules and the total interfacial potential drop across the electrolyte:electrode interface.

Important insights for water flipping can be provided by atomistic simulations^{10–12}, but experimental benchmarks for the number of water molecules that flip, and the associated energetics, have not yet been

¹Department of Chemistry, Northwestern University, Evanston, IL, USA. ²Pacific Northwest National Laboratory, Richland, WA, USA. ³Materials Science Division, Argonne National Laboratory, Lemont, IL, USA. ✉ e-mail: f-geiger@northwestern.edu

obtained. From an experimental perspective, scanning probes^{13,14} have been successfully paired with finite-element analysis¹⁵ and extended to individual molecules¹⁶, including water over ultraflat surfaces¹⁷, to obtain topographic information of liquid:solid interfaces, but the absolute number of net-aligned Stern layer water molecules has not yet been reported from experiments performed on electrodes. Counting how many Stern layer water molecules point their dipoles up vs down requires an interface-selective probe that is also sensitive to the absolute dipole orientation. Experimental methods sensitive to interfacial potentials and fields include fluorescent labeling, which allows for super-resolution but is subject to bleaching within a few minutes¹⁸. Voltage-sensitive spin¹⁹, Stark^{19–28}, or plasmonic labels²⁹ are popular spectroscopic alternative methods, especially when the probe is tethered to an electrode during potential sweeps to avoid label desorption. Despite their surface specificity and sensitivity to interfacial potentials^{30,31}, nonlinear spectroscopic studies of hematite:electrolyte interfaces remain sparse^{32–34}, given the strong absorber problem on both sides of the interface.

In this work, we develop phase- and amplitude-resolved SHG spectroscopy at buried, 10-nm thin Fe₂O₃ nanolayer electrodes prepared by atomic layer deposition (ALD)^{33,34}. We apply external bias along with an absolute phase referencing method to establish the zero SHG phase; employ an optical model to connect the amplitude and phase to the 2nd-order nonlinear susceptibility and the total interfacial potential; and we count the number of net-aligned Stern layer water molecules and quantify the net work associated with water flipping as a

function of applied potential between pH 5 and 13. We find this work to correlate with the Tafel slopes we measure, suggesting that means to lower the work required to flip the Stern layer water molecules could lower the OER's overpotential.

Results and discussion

Figure 1 shows the SHG signal intensity at 516 nm recorded at pH 9, pH 11, and pH 13, along with the measured current, as a function of applied potential against Ag/AgCl balanced to 1M ionic strength with NaClO₄. The SHG intensities exhibit a minimum around 0.4–0.5 V, with lower signal intensities produced at pH 13 when compared to pH 11 or pH 9. The measured current recapitulates that observed by others^{35,36}, in that no iron oxidation/reduction waves are observed and that mA cm⁻² current densities are observed at -1V applied bias in the dark. Control measurements show that the 1033 nm laser illumination does not produce a photocurrent. The FTO-containing slide produces 10–20 counts per 100 ms changes in the SHG intensity during the CVs, ten times smaller than the signals observed from the ALD-hematite on FTO-deposited glass samples (please see Supplementary Information Fig. S1). The current produced by the FTO-deposited glass slide at +1.1V applied bias is about ten times smaller than that obtained from the ALD-hematite on FTO-deposited glass at the same applied voltage (0.8 mA cm⁻², again, in the dark). Changes in the amplitude and phase (obtained as described further below) with applied potential are not resolved when the FTO-deposited glass sample is probed (please see Supplementary

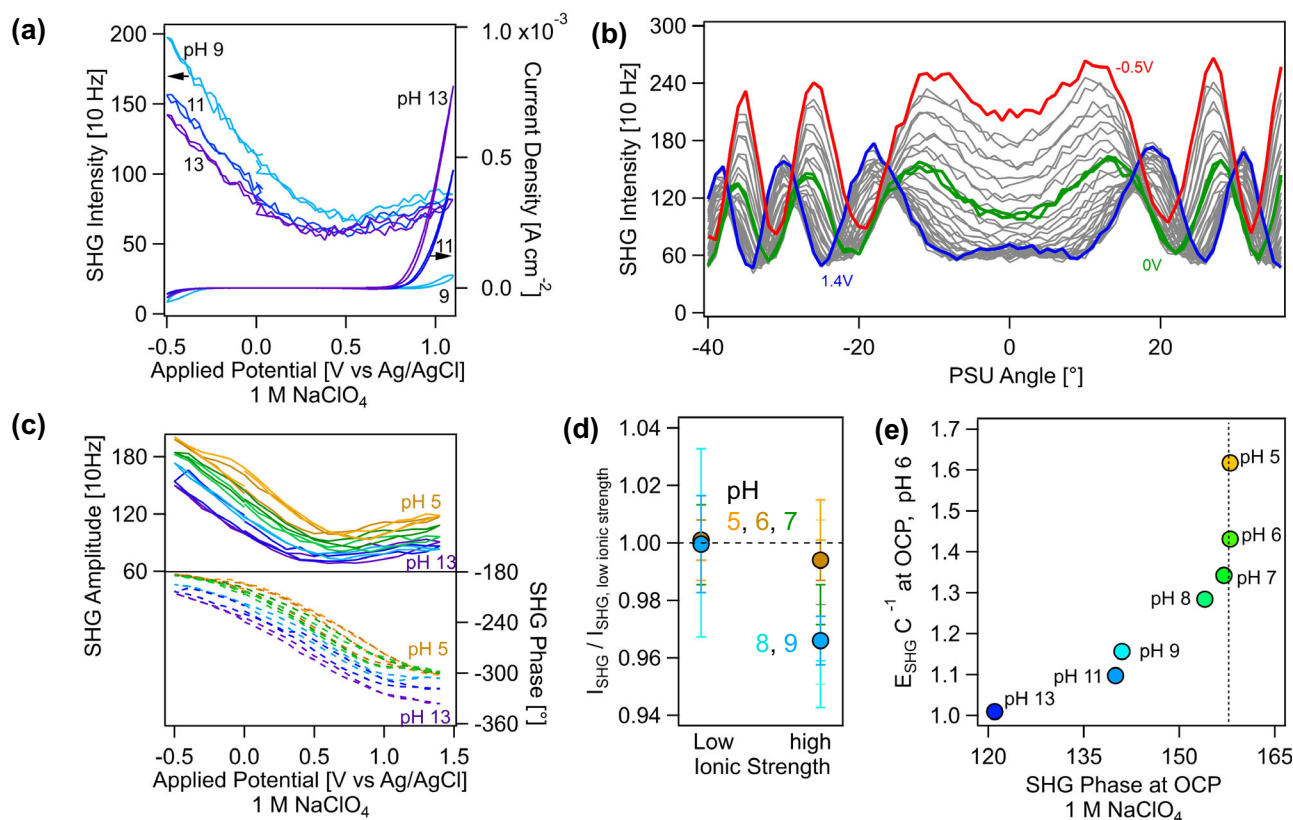


Fig. 1 | SHG Phase and Amplitude Measurements. **a** Second Harmonic Generation (SHG) intensity measured at 100 ms integration time (left) and current density (right) as a function of applied potential at conditions indicated for pH 9 (light blue), 11 (dark blue), and 13 (purple). **b** Interference patterns generated when shifting the phase of the fundamental and second harmonic relative to one another with a phase shifting unit (PSU) recorded at pH 13 and 1 M NaClO₄ at various applied potentials. **c** SHG amplitude (left) and phase (right) as a function of applied potential at conditions indicated for pH 5 (brown), 6 (orange), 7 (green), 8 (very

light blue), 9 (light blue), 11 (dark blue), and 13 (purple). **d** Average SHG Intensity recorded at indicated pH values for low (0.1 mM) and high (0.1 M) ionic strength normalized to the low ionic strength condition at a given pH. The error bars represent the standard deviations in the SHG intensity recorded over 60 s at each given condition for a representative electrode. **e** SHG Amplitude divided by the calibration factor, $C = 4.2 \times 10^{-22} \text{ m}^2 \text{ V}^{-2}$, vs SHG phase at open circuit potential and pH 6 at the pH values indicated. The vertical line highlights the pH conditions where the phase changes minimally.

Information Fig. S1), likely due to the small SHG signal intensities produced by that anode.

Figure 1b shows a representative collection of nonlinear optical interferograms recorded during a cyclic voltammogram (CV) between -0.5 and $+1.4$ V vs Ag/AgCl at pH 13 and 1 M NaClO₄. As a reminder, the interferograms arise from the constructive and deconstructive interaction of the SHG photons generated by the sample (the “signal”) and by a 50 μm thin α-quartz wafer (the “local oscillator”) as their relative phase at the detector is matched and mismatched using a rotating phase shifting unit. Clear changes in the amplitude and phase are observed at the various applied potentials. Figure 1c shows the SHG amplitudes and phases obtained during CVs collected between pH 13 and pH 5 (more acidic conditions lead to FTO dissolution). The SHG phase values from our fit function (please see Supplementary Information Note S1) were converted to the absolute phases relative to the zero phase from the purely real SHG signal produced from a hematite-free portion of our sample. These portions were produced by using a Zn-HCl etching method on as-deposited ALD-hematite-on-FTO substrates. In short, a Kapton mask was used to create a 10 × 15 mm exposed window where Zn metal powder and 2 M HCl were placed. The resulting reaction was allowed to proceed for 20 minutes before removing the excess reactants and rinsing with deionized water. If the window retained any conductivity, the etching process was repeated until only non-conductive glass remained. We first measured an SHG interferogram at a portion of our glass slide that was free of FTO and hematite, then translated the sample stage such that the laser beam impinged on the ALD-hematite-on-FTO-deposited glass portion of our sample in contact with air to measure an interferogram there, and finally added pH 13/1 M NaClO₄ electrolyte using our peristaltic pump so that the optical alignment did not change and a third interferogram could be measured.

Per means of example, the fitted SHG phase for the glass:air interface of the data shown in Fig. 1c was $\varphi_{\text{fit}} = 180^\circ \pm 20^\circ$ from up to seven replicate measurements (please see Supplementary Information Fig. S2 for a representative fringe obtained from the glass:air interface). This result means that the offset needed to obtain the absolute zero phase should be $\varphi_{\text{offset}} = -180^\circ$ since then $\varphi_{\text{fit}} - \varphi_{\text{offset}} = 0^\circ$. This zero phase is expected for a transparent, non-birefringent, uncharged material such as glass, for which $\chi_{\text{glass:air}}^{(2)} \propto E_{\text{SHG, glass:air}} e^{i0^\circ} =$ purely real, which is fulfilled if the SHG phase is 0° . The fitted phase for the ALD-hematite-on-FTO-deposited glass portion of the sample is found to be delayed from 180° to 50° , which corresponds to an absolute phase of $50^\circ - 180^\circ = -130^\circ$. Adding electrolyte at pH 13 further delays the phase by -100° to -55° , which corresponds to an absolute phase of -235° (or $+125^\circ$, given 360° symmetry) for the hematite:electrolyte interface at pH 13 and OCP.

The second-order nonlinear susceptibility should contain contributions from two sources, namely the Stern layer ($\chi_{\text{Stern}}^{(2)}$) and the topmost layer of hematite’s iron and oxygen atoms ($\chi_{\text{hem}}^{(2)}$). Given the slight absorbance of our 10 nm thin hematite nanolayers at around 500 nm (near the SHG wavelength), $\chi_{\text{hem}}^{(2)}$ is likely to be pre-resonant at this wavelength and needs to be isolated and quantified. To do so, we went to a condition of applied potential and pH where the surface and the space charge potentials are minimized, such that the remaining source of SHG is largely due to $\chi_{\text{hem}}^{(2)}$, given that waters’ molecular hyperpolarizabilities should orientationally average to a zero (or close to zero) $\chi_{\text{Stern}}^{(2)}$ value when there is no electric field across the Stern layer. We therefore proceeded to determine, with zero applied potential, the pH of zero charge (PZC, at which the total surface potential should be at or near zero) and the flatband potential, U_{FB} (at which the space charge layer potential should be at or near zero). A Mott-Schottky analysis of electrical impedance spectroscopy (EIS) measurements (please see Supplementary Information Note S2) indicates the flatband potential of our 10-nm thin nanolayers to be -0.2 V (resp. $+0.2$ V) vs Ag/AgCl at 1 M NaClO₄ and pH 13

(resp. pH 6). SHG measurements are consistent with a PZC between 5 and 7, as the SHG intensity change with ionic strength is negligible in that pH range (Fig. 1d), supporting the notion that the PZC at zero applied bias is between pH 5 and 7. Our earlier experiments on ALD-hematite deposited on fused silica (no FTO present) were consistent³³ with a point of zero charge of 5.5 ± 0.3 , in agreement with literature values for “natural” hematite (PZC = 5–7) but below those reported for “commercial” (PZC = 6–9) or “synthetic” (PZC = 7–10) hematite samples^{37–43}. In this present work, we also determine the phase and amplitude via optical interference measurements at each pH (Fig. 1e) and at open circuit potential, finding that the change in the SHG phase is smallest between pH 5 and 7. The phase at the PZC is not zero, as it would be for a fully transparent material. Instead, our hematite nanolayers appear orange and have an absorbance of -0.1 at the 515 nm SHG signal wavelength (please see Supplementary Information Fig. S3). To obtain $\chi_{\text{hem}}^{(2)}$ in Eq. 1, we collected interferograms at pH 6 and pH 7 (covering the PZC range) and at an applied potential of $+0.1$ V and $+0.2$ V, covering the flatband potential range that we determined using EIS in this pH range, and find that $\chi_{\text{hem}}^{(2)} = 3.6 \times 10^{-22} \text{ m}^2 \text{ V}^{-1} \cdot e^{i\varphi_{\text{hem}}}$ with $\varphi_{\text{hem}} = 150^\circ - 180^\circ$ (from replicate measurements on three different electrodes, again, relative to the zero phase from the glass:air interface). The remaining contribution to the effective second-order nonlinear susceptibility, $\chi_{\text{Eff}}^{(2)}$, at high ionic strength (1 M NaClO₄), where the Debye length is less than one nanometer, is then just $\chi_{\text{hem}}^{(2)}$, the second-order nonlinear susceptibility of the hematite:Stern layer interface and its associated phase, φ_{hem} , according to

$$\chi_{\text{Eff}}^{(2)} = C \cdot E_{\text{sig}} e^{i\varphi_{\text{sig}}} = \chi_{\text{Stern}}^{(2)} + \overline{\chi_{\text{hem}}^{(2)}} - (1 + 1.5i)\chi_{\text{water}}^{(3)} \cdot \Phi(0)_{\text{DL}} \pm \chi_{\text{SC}}^{(3)} \cdot \frac{U - U_{\text{FB}}}{d_{\text{SC}}} \int_{-\delta}^0 e^{i\Delta k_z z} dz \quad (1)$$

with $\chi_{\text{Stern}}^{(2)}$, $\Phi(0)_{\text{DL}}$, and $U - U_{\text{FB}}$ all zero at the PZC and 0.1–0.2 V applied. (Eq. 1). Here, the horizontal bar indicates that hematite’s second-order response is complex-valued due to partial resonance enhancement as outlined below, C is the quartz calibration factor that also includes the Fresnel coefficients (C is determined to be $4.2 \times 10^{-22} \text{ m}^2 \text{ V}^{-1}$ for our hematite on FTO-coated glass anodes, at pH 7 and OCP)⁴⁴, and the $\chi_{\text{water}}^{(3)}$ term accounts for the phase-matched third-order nonlinear polarization in the bulk water, as described earlier^{45–50}. This term was shown by Wen et al. to be invariant with pH, ionic strength, and surface composition⁴⁸, so we treat it to be invariant with applied potential as well. The last term is the third-order nonlinear polarization in the space charge layer, with the difference of externally applied potential, U , and the flatband potential, U_{FB} , over the space charge layer thickness, d_{SC} (limited to the 10 nm thickness of the hematite nanolayers) multiplied into the third-order nonlinear susceptibility of the space charge layer, $\chi_{\text{SC}}^{(3)}$, and the phase-matching term arising in the hematite nanolayer having an effective thickness of δ . We note that recent work by Lian and co-workers⁵¹ writes a similar expression summing the $\chi^{(2)}$ contribution with the $\chi^{(3)}$ contributions from the space charge and diffuse layers, in their case of a TiO₂ anode, albeit without the required phase matching term.

We now rearrange Eq. 1 by subtracting $\chi_{\text{hem}}^{(2)}$ from $C \cdot E_{\text{sig}} e^{i\varphi_{\text{sig}}}$ and solve the integral on the right-hand-side by employing a lower bound of $\delta = 20$ nm, given the AFM-derived 10 nm rms roughness of our hematite nanolayers on FTO, a wave vector mismatch Δk_z of $2.5 \times 10^7 \text{ m}^{-1}$, and $d_{\text{SC}} = 10$ nm, according to

$$C \cdot E_{\text{sig}} e^{i\varphi_{\text{sig}}} - \overline{\chi_{\text{hem}}^{(2)}} = \chi_{\text{Stern}}^{(2)} - (1 + 1.5i)\chi_{\text{water}}^{(3)} \cdot \Phi(0)_{\text{DL}} \pm (1.9 + 0.5i)\chi_{\text{SC}}^{(3)} \cdot (U - U_{\text{FB}}) \quad (2)$$

We use water's third-order nonlinear susceptibility, $\chi_{water}^{(3)} = 1 \times 10^{-21} \text{ m}^2 \text{ V}^2$ for non-resonant conditions^{46,52–56}, and the EIS-derived space charge layer thickness estimate, d_{SC} , of 10 nm. Third-order nonlinear susceptibilities of iron oxide nanolayers have been reported to be sizeable from Maker fringe measurements in transmission geometries^{57–59}. Our own measurements of 1030 nm \rightarrow $\lambda(\text{THG}) = 344$ nm (recorded at pH 13 and OCP in our internal reflection geometry after replacing the 515 bandpass filter with a 325 ± 25 nm bandpass filter, Edmund Optics 12094) indicate a few tens of counts per 100 msec, whereas the SHG signal intensity for 1030 nm \rightarrow $\lambda(\text{SHG}) = 515$ nm is in the few hundred counts per 100 msec range. The square root of this intensity ratio (-3) is close to the one we obtain from a complementary measurement using a tunable near-infrared laser (1kHz-pumped TOPAS, 120 fs bandwidth, 10 μJ per pulse), which allows us to measure the intensity at a third harmonic wavelength (1500 nm \rightarrow 550 nm) that matches the second harmonic wavelength (1100 nm \rightarrow 550 nm, close to the 516 nm SHG wavelength used in our oscillator experiments described throughout this work). That latter experiment yields a square root of the THG and SHG intensity ratio at 550 nm of -6. Both experiments indicate that $\chi_{SC}^{(3)}$ in our 515 nm amplitude and phase resolved SHG experiments is on the order of 10^{-22} – $10^{-21} \text{ m}^2 \text{ V}^{-2}$, given that $\chi_{hem}^{(2)} = 3.6 \times 10^{-22} \text{ m}^2 \text{ V}^{-1}$. Additional measurements show that the third harmonic of 1030 nm is invariant with applied potential. This result supports the notion that $\chi_{SC}^{(3)}$ and its thickness is independent of applied potential on our 10 nm thin hematite nanolayers.

We now convert Eq. 2 into the properties we seek, namely $\chi_{Stern}^{(2)}$ (the nonlinear susceptibility of the Stern layer species, largely H_2O , with some minor amount of counter ions) and $\Phi(0)$ (the total interfacial potential drop across it). To this end, we collect *Re* and *Im* of Eq. 2 and find

$$\Phi(0) = - \left[C \cdot E_{\text{sig, norm}} \sin(\varphi_{\text{sig}}) - \chi_{hem}^{(2)} \sin(\varphi_{hem}) - 0.5 \cdot \chi_{SC}^{(3)} \cdot (U - U_{FB}) \right] / 1.5 \chi_{water}^{(3)} \quad (3a)$$

and

$$\chi_{Stern}^{(2)} = C \cdot E_{\text{sig, norm}} \cos(\varphi_{\text{sig}}) - \chi_{hem}^{(2)} \cos(\varphi_{hem}) + \chi_{water}^{(3)} \cdot \Phi(0) - 1.9 \chi_{SC}^{(3)} (U - U_{FB}) \quad (3b)$$

Here again we use the following parameters: $C = 4.2 \times 10^{-22} \text{ m}^2 \text{ V}^{-1}$, $\chi_{hem}^{(2)} = 3.6 \times 10^{-22} \text{ m}^2 \text{ V}^{-1} \cdot e^{i\varphi_{hem}}$ with $\varphi_{hem} = 150^\circ$ – 180° relative to the 0 phase of the glass:air interface, $\chi_{water}^{(3)} = 1 \times 10^{-21} \text{ m}^2 \text{ V}^2$, $U_{FB} = -0.2$ V vs Ag/AgCl at pH 13, and $\chi_{SC}^{(3)}$ is on the order of 10^{-22} – $10^{-21} \text{ m}^2 \text{ V}^{-2}$. We employ pH 7 at OCP as the reference state for which we determined our calibration factor *C* and to which we normalize the SHG amplitudes in the form of $E_{\text{sig, norm}}$.

Figure 2a shows the total surface potential, $\Phi(0)$, and the Stern layer second-order nonlinear susceptibility, $\chi_{Stern}^{(2)}$, at pH 13. The total surface potential is slightly negative at OCP, consistent with surface potentials around -0.1 to -0.2 V at elevated pH that were reported for

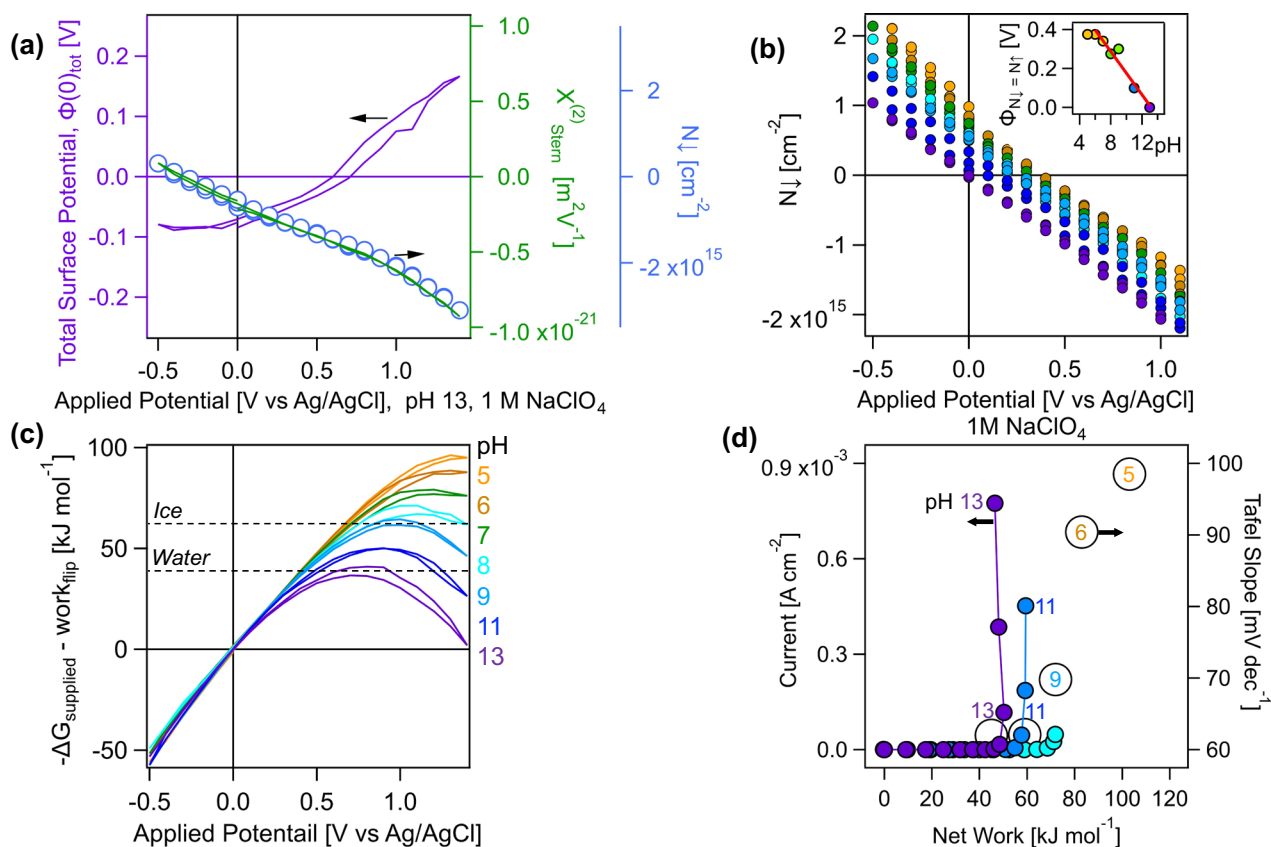


Fig. 2 | From amplitude and phase to number of net-aligned water molecules, total potential, and work to flip water. **a** Total potential (purple line, left ordinate), second order nonlinear susceptibility (green line, right ordinate), and number of net-aligned Stern layer water molecules (circles, blue right ordinate) as a function of applied potential at pH 13 and 1 M NaClO_4 . **b** Number of net-aligned Stern layer water molecules pointing their oxygen atoms towards the electrode as a function of applied potential for pH values indicated and Stern slope result (inset). **c** Net work associated with water flipping as a function of applied potential at indicated pH values. The dashed lines indicate the cohesive energies of water (top) and ice (bottom). **d** Current density measured at pH 13, 11, and 9 (left ordinate) and Tafel slopes measured at pH 13, 11, 9, 7, 6, and 5 (right ordinate) plotted against the net work associated with Stern layer water flipping.

The number of net-aligned water molecules was calculated with the following equation: $N_{\downarrow} = \chi_{Stern}^{(2)} \cdot \epsilon \epsilon_0 (10^4 \text{ cm}^2 \text{ m}^{-2} \text{ a}^{(2)})^{-1}$. **c** Net work associated with water flipping as a function of applied potential at indicated pH values. The dashed lines indicate the cohesive energies of water (top) and ice (bottom). **d** Current density measured at pH 13, 11, and 9 (left ordinate) and Tafel slopes measured at pH 13, 11, 9, 7, 6, and 5 (right ordinate) plotted against the net work associated with Stern layer water flipping.

various hematite crystal faces using electrochemical and modeling means⁶⁰. At +0.6 V applied bias, the total surface potential crosses zero V to become positive, increasing up to +400 mV at +1.4 V applied bias. The $\chi_{Stern}^{(2)}$ values, in turn, are positive for negative applied potentials up to 0 V applied, beyond which they turn negative, consistent with the flipping of the Stern layer water molecules from a “protons toward the electrode” to a “protons away from the electrode” configuration. Generally, $\chi_{Stern}^{(2)}$ values of water molecules pointing their protons away from bulk water are positively signed, as observed in phase-resolved vibrationally resonant sum frequency generation spectroscopy studies^{31,61,62} and in angle-resolved non-resonant second harmonic scattering experiments⁵⁵. We then employ our previously established equation^{52,63} to estimate the number of net-aligned Stern layer water molecules, $N_{\downarrow} = \chi_{Stern}^{(2)} \cdot \epsilon \epsilon_0 (10^4 \text{ cm}^2 \text{ m}^{-2} \alpha^{(2)})^{-1}$, where we use a Stern layer water permittivity ϵ of 1.77–2⁶⁴, ϵ_0 is the vacuum permittivity, and $\alpha^{(2)} = 4.2 \times 10^{-52} \text{ C m}^3 \text{ V}^{-2}$ is the $\alpha_{xxz}^{(2)} = \alpha_{yzz}^{(2)}$ tensor element estimate obtained from MP4-level calculations of the second-order molecular hyperpolarizabilities of a pure liquid water water^{53,54} to which our polarization combination is sensitive. Given our 1 M aqueous solution of NaClO₄, we expect some amount of counter ions to be present in the Stern layer, but the most abundant species is H₂O. While the distribution function of the interfacial molecular dipoles is not known, the simplest treatment (a two-state model) provides an upper estimate of the number of net-aligned Stern layer water molecules, which corresponds to physically reasonable number densities and energy estimates, as we will show below. Yet, we caution that our point estimates for the number of Stern layer water molecules is an upper estimate, given that they are likely subject to a mono- or multimodal orientation distribution, and given that the Stern layer water density differs from that of the bulk^{65,66}.

Figure 2a shows that the largest $\chi_{Stern}^{(2)}$ values, at +1.4 V applied, correspond to -1 monolayer of net-aligned water molecules (10^{15} cm^{-2} , based on water's density at room temperature and standard pressure) pointing their oxygen atoms towards the electrode and their protons into the bulk electrolyte. As shown in Supplementary Information Fig. S4, these results change somewhat for $\chi_{SC}^{(3)}$ values between $4 \times 10^{-22} \text{ m}^2 \text{ V}^{-2}$ and $8 \times 10^{-22} \text{ m}^2 \text{ V}^{-2}$, with the larger values resulting in $\chi_{Stern}^{(2)}$ values of $1.5 \times 10^{-21} \text{ m}^2 \text{ V}^{-1}$ at +1.4 V applied. We consider these larger $\chi_{Stern}^{(2)}$ values unreasonable as they would correspond to 5 full monolayers of water molecules flipping (the 0.7 nm Debye length at 1 M ionic strength corresponds to -7 water monolayers). Supplementary Information Fig. S5 shows that changing the lower integration limit of the $\chi_{SC}^{(3)}$ term in Eq. 1 from 20 nm (given the rms roughness from AFM) to 10 nm (the space charge layer thickness from the Mott-Schottky analysis of the EIS data) yields qualitatively similar (albeit somewhat smaller) values if $\chi_{SC}^{(3)} = 8 \times 10^{-22} \text{ m}^2 \text{ V}^{-2}$.

Figure 2b shows the number of net-aligned Stern layer water molecules as a function of applied potential up to 1 V for the pH values we surveyed between pH 5 and 13. The results indicate that water flipping requires higher positive potentials at lower pH values. As shown in the inset of Fig. 2b, the total surface potential at which the same number of Stern layer water molecules points up versus down at zero applied bias (OCP) exhibits Nernstian behavior, given its pH-dependent slope of $0.055 \pm 0.006 \text{ V pH}^{-1}$.

The work associated with Stern layer water flipping is computed by multiplying N_{\downarrow} by the Faraday constant and $\Phi(0)$, followed by division through $1 \times 10^{15} \text{ cm}^{-2}$ (the water monolayer) and another division by Avogadro's number. Figure 2c plots the difference of the free energy provided by the electrode potential, obtained by multiplying Faraday's constant, F , with the applied potential, U , and the work associated with Stern layer water flipping. Figure 2c indicates that it requires the least amount of work to flip the Stern layer water molecules at the highest pH. Moreover, as the pH is increased from 5 to 13, the net work associated with water flipping decreases from one

exceeding the cohesive energy of ice⁶⁷ by multiple tens of kJ mol^{-1} to one matching the cohesive energy of liquid water. Figure 2d shows that it is at these high pH values that the OER current density is highest, whereas it is significantly smaller at pH 11 and 9, and even absent at the lowest pH values studied here. Tafel slopes (please see Supplementary Note S3 and Supplementary Information Fig. S6) recorded in the several potential ranges recapitulate this result as well: they are lowest when the net work to flip the Stern layer water molecules is lowest (Fig. 2d).

In conclusion, our work shows that nonlinear optical amplitude and phase measurements provide new insights into the surface processes involving interfacial water molecules before and during water oxidation. We separate the detected SHG response into four distinct contributions, namely the second-order nonlinear susceptibility of the Stern layer water molecules, that of the hematite surface species, the third-order nonlinear susceptibility of the diffuse layer water molecules, and that of the space charge layer within hematite. Our optical model provides estimates for the number of net-aligned Stern layer water molecules and the total electrostatic potential across the hematite:electrolyte interface.

The model employs well-established inputs from experiment and theory with regards to $\chi_{water}^{(3)}$. Using an absolute phase determination method that involves the determination of the absolute zero phase from a non-birefringent, transparent, and uncharged reference material (glass), we quantify the $\chi^{(2)}$ of hematite, $\chi_{hem}^{(2)}$, and its associated phase at the point of zero charge and the flat band potential (pH 6 and +0.2 V vs Ag/AgCl at 1 M NaClO₄). Estimates for $\chi^{(3)}$ of the space charge layer, $\chi_{SC}^{(3)}$, are derived from third- and second harmonic generation measurements at various wavelengths. The model is then run within the upper and lower bounds of this estimate, along with two estimates for the lower integration bound of the space charge layer integral in Eq. 1 ($\delta = 10$ and 20 nm).

Our results across five electrodes indicate that -1–2 monolayers of water are net-aligned, pointing the oxygen atoms towards the surface at the highest positive potentials applied. Free energy relationships establish that the work associated with water flipping is least at the highest pH, with a free energy gain of $-6.1 \pm 0.1 \text{ kJ mol}^{-1} \text{ pH}^{-1}$. The pH-dependence of the potentials at which the Stern layer water molecules start to flip at zero applied bias is Nernstian. Once the applied bias is such that the net work associated with water flipping matches the cohesive energy of liquid water, the OER takes off, as indicated by the current density increase at pH 13. At lower pH values, the net work needed to flip the Stern layer water molecules increases beyond that of the cohesive energy of ice (at pH 9), where the OER current is much smaller than at pH 13 and approaches 100 kJ mol^{-1} at pH 5, where the OER current is negligible.

Like the invariance of $\chi_{water}^{(3)}$ to pH, [salt], and surface composition⁴⁸, we expect $\chi_{SC}^{(3)}$ to be invariant with applied potential. Indeed, our own measurements show that the THG signals we obtain from our electrodes are invariant with applied potential. However, we caution that one assumption made in our optical model is perhaps not appropriate at applied potentials leading to significant oxygen evolution, namely that $\chi_{hem}^{(2)}$ is constant. In other work that will be reported in due course we find SHG signals at $\lambda(\text{SHG}) = 550\text{--}570 \text{ nm}$ that grow in intensity with applied potential, clearly indicating that $\chi_{hem}^{(2)}$ changes, as these wavelengths correspond to the λ_{max} of high-oxidation state iron species (ferryl and ferrates) that form at the applied potential when the oxidation current increases parabolically (+0.6 V or so). However, at 515 nm the SHG response is dominated by the second-order nonlinear susceptibility of the Stern layer water molecules.

In sum, we report new physical insights into the structure, electrostatics, and thermodynamics of the Stern layer water molecules before and during the oxygen evolution reaction over thin hematite nanolayer anodes. Our findings suggest a causal relationship between Stern layer water flipping and the OER overpotential. We expect the

approach to be useful for contributing to the understanding of the molecular origin underlying the high overpotential associated with the oxygen evolution reaction on hematite. Future work is geared towards following water flipping under conditions of visible light illumination, quantifying the wavelength dependences of the nonlinear optical resonances under applied potential, and exploring other catalytic surfaces such as those prepared from platinum group elements.

Methods

Phase-resolved second harmonic generation spectrometer

We probe 10-nm thin hematite layers deposited by ALD onto fluorine-doped tin oxide (FTO)-deposited float glass slides with the 80 fs, 1033 nm output of an 80 MHz ytterbium crystal-based oscillator (LightConversion Flint, 12 nm bandwidth). The conductive FTO substrate + hematite nanolayer is used as the working electrode in a standard three electrode cell configured for optical spectroscopic interrogation. Unlike prior studies employing macroscopically thick electrodes^{12,32,68–70}, the 10 nm thin layers produce 3rd-order bulk signals that are comparable in magnitude to the 2nd-order response from the interface, as we show further below, making our approach quite sensitive to the processes occurring at the electrode:electrolyte interface.

In order to obtain the number of net-aligned water molecules in the Stern layer and the total interfacial potential across the hematite:electrolyte interface, we employ a nonlinear optical spectrometer that provides the SHG amplitude and phase. The spectrometer is shrouded to minimize dark counts to ~ 10 per 100 ms. A longpass filter (Thorlabs FELH0750) blocks any residual visible radiation with wavelength less than 750 nm. The input polarization is set to be parallel to the surface (“s-in”), and we defocus gently using a 10 cm lens pulled back by 3 cm from its focal point, delivering 400 mW of input power. We block the fundamental and any SHG from the external sample window surface using an anodized aluminum plate and direct the fundamental and the SHG signal from the electrode:electrolyte interface into a heterodyning assembly that is separately shrouded so that the dark counts measured using our photomultiplier/single photon counter assembly is minimized. We spectrally isolate the 516 nm SHG signal using a bandpass filter (Thorlabs, FBH520-40) and record its p-polarized signal intensity. The SHG amplitude and phase are obtained by interfering the signal from the sample with a local oscillator produced in a 50 μm thin α -quartz wafer as a function of rotational angle of a phase shifting unit consisting of a 1 mm fused silica plate on a motorized rotational stage⁶³. The resulting interference patterns are then fit using the function described in Supplementary Note S1 providing the amplitude and phase of the SHG. The amplitude and phase are then input into our optical models to calculate the relevant quantities.

Nanolayer synthesis and characterization

The hematite nanolayers are prepared as follows: commercial FTO glass substrates (part number CG-14FTO-1109, obtained from Delta Technologies, Colorado) are float glass slides onto which a few 100 nm of pyrolytic FTO are deposited by chemical vapor deposition. We prepare hematite thin films on these FTO-coating glass slides using a $\text{Fe}(\text{Cp})_2$ and O_3 process as described previously³³, only slightly modified with longer exposure to $\text{Fe}(\text{Cp})_2$ while the vacuum pump is gated from the chamber. $\text{Fe}(\text{Cp})_2$ (Sigma, 98%) was maintained at 100 °C while O_3 was generated using corona discharge in ultra-high purity O_2 (LG-7, Ozone Engineering) operating at 40% power. The ALD recipe is expressed as $(t_1 - t_2 - t_3)_2 - (t_4 - t_5)_3$, where t_1 and t_4 are the dose times for $\text{Fe}(\text{Cp})_2$ and O_3 precursor respectively, t_2 is the exposure time for the $\text{Fe}(\text{Cp})_2$ precursor, and t_3 and t_5 are N_2 purge periods. The complete ALD process was $(6 - 34 - 80)_2 - (60 - 60)_3$ where the t_1 pulse time was 6 s and the t_2 wait time was 34 s, leading to a total exposure time of 40 s.

The t_4 O_3 pulse time was 60 s, and the purge times t_3 and t_5 were 80 s and 60 s respectively. The $\text{Fe}(\text{Cp})_2$ exposure-purge cycle was performed 2x times before exposure to three O_3 pulse-purge cycles. This method yielded a growth rate of ranging from 0.75 to 1.0 \AA per cycle depending on the distance of the substrate from the inlet. Insufficient purging of the $\text{Fe}(\text{Cp})_2$ precursor can produce uneven film growth on the substrate backside, which could affect spectral analysis. With sufficient purging, the backside growth rate was measured to be $\sim 50\%$ of the growth rate on the top side of the substrate. All films were deposited to a thickness of 10 nm as confirmed by ellipsometry of silicon witness samples and an optical absorption vs thickness calibration curve (please see Supplementary Information Fig. S7).

X-ray photoelectron spectroscopy and atom probe tomography show high chemical purity in our ALD hematite nanolayers³³. Supplementary Information Fig. S7b, c show a depth-resolved elemental analysis indicating no fluorine in the top-most region of our 10-nm hematite layers. While the semiconducting ALD-hematite nanolayers exhibit no measurable conductivity when measured on an insulating substrate, the ALD-hematite-on-FTO-deposited glass samples show a combined resistance of a few tens to a few hundred $\text{Ohm}/\text{sq.}$, consistent with the FTO-coated glass substrates from Delta Technologies. The samples resist delamination or corrosion, even in 0.6 M salt concentration⁷¹. X-Ray photoelectron spectroscopy and grazing incidence angle X-ray diffraction are consistent with hematite (Fe/O ratio of between 0.64 and 0.73, multiplet in the Fe $2p_{3/2}$ region, and major 2 θ peaks at 33–35, 49, and 54°)³³. Atomic force microscopy shows an rms surface roughness nearly identical to that of the FTO-deposited glass slides (10 nm, please see Supplementary Information Note S4).

Spectroelectrochemical cell and measurements

The sample cell is described elsewhere⁶³. Briefly, the assembly consists of custom-built PEEK-based half-cells, one holding a 1 mm-thin optical window and the other holding an ALD-hematite on FTO-deposited glass slide, both held leak tight using O-rings (FFKM perfluoroelastomer, Ace Seal). We use a sealed 4 mm diameter, 30 mm long Ag/AgCl reference electrode (SNG-ECRXACC30, redox.me) located in the same compartment as the working (ALD-hematite on FTO-deposited glass) and counter (Pt) electrodes. An inlet and outlet allow for liquid exchange using a peristaltic pump so that we can vary the pH under *operando* conditions. The electrochemical measurements are carried out with a PGSTAT302N electrochemical workstation with a SCAN250 analog linear sweep module (Metrohm). CVs were ran between -0.5 V and 1.4 V (V vs Ag/AgCl) at a scan rate of 0.05 V s^{-1} prior to any measurements until the SHG response was consistent. The electrodes in the cell has ~ 3.9 cm^2 area exposed (corresponding to a mass loading of 5.2×10^{-6} g cm^{-2}) to electrolyte leaving the remain section of glass accessible for phase referencing. The SHG amplitude and phase measurements presented in this dataset were carried out on twelve different hematite anodes. Among those twelve, the pH titrations were carried out on four different hematite anodes.

Data availability

The source data presented in this study have been deposited in the figshare database under access code <https://doi.org/10.6084/m9.figshare.28592531.v1>⁷².

References

1. Riha, S. C. et al. Atomic layer deposition of a submonolayer catalyst for the enhanced photoelectrochemical performance of water oxidation with hematite. *ACS Nano* **7**, 2396–2405 (2013).
2. Xiao, J. et al. Suppressing the electron-hole recombination rate in hematite photoanode with a rapid cooling treatment. **350**, 48–55 (2017).

3. Li, F. et al. Recent advances on interfacial engineering of hematite photoanodes for viable photo-electrochemical water splitting. *Eng. Rep.* **3**, e12387 (2021).
4. Nguyen, H. C., Garcés-Pineda, F. A., de Fez-Febre, M., Galan-Mascaros, J. R. & Lopez, N. Non-redox doping boosts oxygen evolution electrocatalysis on hematite. *Chem. Sci.* **11**, 2464–2471 (2020).
5. Eggleston, C., Shankle, A. J. A., Moyer, A. J., Cesar, I. & Graetzel, M. Anisotropic photocatalytic properties of hematite. *Aquat. Sci.* **71**, 151–159 (2009).
6. Strmcnik, D. et al. The role of non-covalent interactions in electrocatalytic fuel-cell reactions on platinum. *Nat. Chem.* **1**, 466–472 (2009).
7. Li, J., Chen, H., Triana, C. A. & Patzke, G. R. Hematite photoanodes for water oxidation: electronic transitions, carrier dynamics, and surface energetics. *Angew. Chem. Int. Ed.* **60**, 18380–18396 (2021).
8. Liu, Y., Le Formal, F., Boudoire, F. & Guijarro, N. Hematite photoanodes for solar water splitting: a detailed spectroelectrochemical analysis on the pH-dependent performance. *ACS Appl Mater. Inter.* **2**, 6825–6833 (2019).
9. Sivula, K., Le Formal, F. & Graetzel, M. Solar water splitting: progress using hematite (α -Fe₂O₃) photoelectrodes. *ChemSusChem* **4**, 432–449 (2011).
10. Shah, A. H. et al. Platinum surface water orientation dictates hydrogen evolution reaction kinetics in alkaline media. *J. Am. Chem. Soc.* **146**, 9623–9630 (2024).
11. Futera, Z. & English, N. J. Water breakup at Fe₂O₃–hematite/water interfaces: influence of external electric fields from nonequilibrium ab initio molecular dynamics. *J. Phys. Chem. Lett.* **12**, 6818–6826 (2021).
12. Xu, P. et al. Cation modifies interfacial water structures on platinum during alkaline hydrogen electrocatalysis. *J. Am. Chem. Soc.* **146**, 2426–2434 (2024).
13. Nellist, M. R. et al. Potential-sensing electrochemical atomic force microscopy for in operando analysis of water-splitting catalysts and interfaces. *Nat. Energy* **3**, 46–52 (2018).
14. Mattei, M. et al. Tip-enhanced raman voltammetry: coverage dependence and quantitative modeling. *Nano Lett.* **17**, 590–596 (2017).
15. Yang, Y., Mayer, K. M., Wickremasinghe, N. S. & Hafner, J. H. Probing the lipid membrane dipole potential by atomic force microscopy. *Biophys. J.* **95**, 5193–5199 (2008).
16. Hapala, P. et al. Mapping the electrostatic force field of single molecules from high-resolution scanning probe images. *Nat. Commun.* **7**, 11560 (2016).
17. Nakouzi, E. et al. Moving beyond the solvent-tip approximation to determine site-specific variations of interfacial water structure through 3D force microscopy. *J. Phys. Chem. C* **125**, 1282–1291 (2021).
18. Wang, Y., Cao, Z., Yang, Q., Guo, W. & Su, B. Optical methods for studying local electrochemical reactions with spatial resolution: a critical review. *Anal. Chim. Acta* **1074**, 1–15 (2019).
19. Voinov, M. A., Rivera-Rivera, I. & Smirnov, A. I. Surface electrostatics of lipid bilayers by EPR of a pH-sensitive spin-labeled lipid. *Biophys. J.* **104**, 106–116 (2013).
20. Bhattacharya, D. et al. Vibrational Stark shift spectroscopy of catalysts under the influence of electric fields at electrode–solution interfaces. *Chem. Sci.* **12**, 10131–10149 (2021).
21. Gunathunge, C. M., Li, J., Li, X. & Waegeler, M. M. Surface-adsorbed CO as an infrared probe of electrocatalytic interfaces. *ACS Catal.* **10**, 11700–11711 (2020).
22. Sarkar, S., Maitra, A., Banerjee, S., Thoi, V. S. & Dawlaty, J. M. Electric fields at metal–surfactant interfaces: a combined vibrational spectroscopy and capacitance study. *J. Phys. Chem. B* **124**, 1311–1321 (2020).
23. Sarkar, S. et al. Mechanistic insights about electrochemical proton-coupled electron transfer derived from a vibrational probe. *J. Am. Chem. Soc.* **143**, 8381–8390 (2021).
24. Baldelli, S. Probing electric fields at the ionic liquid–electrode interface using sum frequency generation spectroscopy and electrochemistry. *J. Phys. Chem. B* **109**, 13049–13051 (2005).
25. Sorensen, S. A., Patrow, J. G. & Dawlaty, J. M. Solvation reaction field at the interface measured by vibrational sum frequency generation spectroscopy. *J. Am. Chem. Soc.* **139**, 2369–2378 (2017).
26. Piontek, S. M. et al. Probing heterogeneous charge distributions at the α -Al₂O₃(0001)/H₂O interface. *J. Am. Chem. Soc.* **142**, 12096–12105 (2020).
27. Ge, A. et al. Interfacial structure and electric field probed by in situ electrochemical vibrational stark effect spectroscopy and computational modeling. *J. Phys. Chem. C* **121**, 18674–18682 (2017).
28. Garcia Rey, N. & Dlott, D. D. Studies of electrochemical interfaces by broadband sum frequency generation. *J. Electroanal. Chem.* **800**, 114–125 (2017).
29. Li, C.-Y. et al. In situ probing electrified interfacial water structures at atomically flat surfaces. *Nat. Mat.* **18**, 697–701 (2019).
30. Bañuelos, J. L. et al. Oxide–and silicate–water interfaces and their roles in technology and the environment. *Chem. Rev.* **123**, 6413–6544 (2023).
31. Rehl, B. et al. Water structure in the electrical double layer and the contributions to the total interfacial potential at different surface charge densities. *J. Am. Chem. Soc.* **144**, 16338–16349 (2022).
32. Saeed, K. H. et al. Monitoring interfacial electric fields at a hematite electrode during water oxidation. *Chem. Sci.* **14**, 3182–3189 (2023).
33. Jordan, D. S. et al. Second harmonic generation studies of Fe(II) interactions with hematite (α -Fe₂O₃). *J. Phys. Chem. C* **117**, 4040–4047 (2013).
34. Troiano, J. M., Jordan, D. S., Hull, C. J. & Geiger, F. A. Interaction of Cr(III) and Cr(VI) with hematite studied by second harmonic generation. *J. Phys. Chem. C* **117**, 5146–5171 (2013).
35. Zandi, O., Schon, A. R., Hajibabaei, H. & Hamman, T. W. Enhanced charge separation and collection in high-performance electro-deposited hematite films. *Chem. Mat.* **28**, 765–771 (2015).
36. Klahr, B. & Hamman, T. W. Water oxidation on hematite photoelectrodes: insight into the nature of surface states through in situ spectroelectrochemistry. *J. Phys. Chem. C* **118**, 10393–10399 (2014).
37. Kosmulski, M. *Properties of Material Surfaces* (CRC Press and Marcel Dekker, 2001).
38. Ahmed, S. M. & Maksimov, D. Studies of the oxide surfaces at the liquid–solid interface. Part II. Fe oxides. *Can. J. Chem.* **46**, 3841–3846 (1968).
39. Das, M. R., Bordoloi, D., Borthakur, P. C. & Mahiuddin, S. Kinetics and adsorption of benzoate and salicylate at the natural hematite–water interface. *Colloids Surf. A* **254**, 49–55 (2005).
40. Joy, A. S., Watson, D. & Cropton, R. W. G. Collector adsorption and surface charge density. *Trans. AIME* **129**, 5–7 (1964).
41. Song, Q. Y., Xu, F. & Tsai, S. C. Magnetic seeding flocculation of weakly magnetic iron minerals. *Int. J. Miner. Process.* **34**, 219–229 (1992).
42. Wang, Y., Pugh, R. J. & Forssberg, E. The influence of interparticle surface forces on the coagulation of weakly magnetic mineral ultrafines in a magnetic field. *Colloids Surf. A* **90**, 117–133 (1994).
43. Yuhua, W. & Jianwei, R. The flotation of quartz from iron minerals with a combined quaternary ammonium salt. *Int. J. Miner. Process.* **77**, 116–122 (2005).
44. Chang, H. et al. Direct measurement of charge reversal on lipid bilayers using heterodyne-detected second harmonic generation spectroscopy. *J. Phys. Chem. B* **124**, 641–649 (2020).

45. Ma, E. et al. A new imaginary term in the 2nd order nonlinear susceptibility from charged interfaces. *J. Phys. Chem. Lett.* **12**, 5649–5659 (2021).
46. Dalstein, L., Chiang, K.-Y. & Wen, Y.-C. Direct quantification of water surface charge by phase-sensitive second harmonic spectroscopy. *J. Phys. Chem. Lett.* **10**, 5200–5205 (2019).
47. Ohno, P. E., Wang, H.-f & Geiger, F. M. Second-order spectral line-shapes from charged interfaces. *Nat. Commun.* **8**, 1032 (2017).
48. Wen, Y.-C. et al. Unveiling microscopic structures of charged water interfaces by surface-specific vibrational spectroscopy. *PRL* **116**, 016101 (2016).
49. Ohno, P. E., Saslow, S. A., Wang, H., Geiger, F. M. & Eienthal, K. B. Phase referenced nonlinear spectroscopy of the alpha-quartz/water interface. *Nat. Commun.* **7**, 13587 (2016).
50. Gonella, G., Lütgebaucks, C., de Beer, A. G. F. & Roke, S. Second harmonic and sum frequency generation from aqueous interfaces is modulated by interference. *J. Phys. Chem. C* **120**, 9165–9173 (2016).
51. Zhao, F. et al. A contactless in situ EFISH method for measuring electrostatic potential profile of semiconductor/electrolyte junctions. *J. Chem. Phys.* **161**, 094703 (2024).
52. Chang, H., Lozier, E. H., Ma, E. & Geiger, F. M. Quantification of stern layer water molecules, total potentials, and energy densities at fused silica: water interfaces for adsorbed alkali chlorides, CTAB, PFOA, and PFAS. *J. Phys. Chem. A* **127**, 8404–8414 (2023).
53. Levine, B. F. & Bethea, C. G. Effects on hyperpolarizabilities of molecular interactions in associating liquid mixtures. *J. Chem. Phys.* **65**, 2429–2438 (1976).
54. Gubskaya, A. V. & Kusalik, P. G. The multipole polarizabilities and hyperpolarizabilities of the water molecule in liquid state: an ab initio study. *Mol. Phys.* **99**, 1107–1120 (2001).
55. Lütgebaucks, C., Gonella, G. & Roke, S. Optical label-free and model-free probe of the surface potential of nanoscale and microscopic objects in aqueous solution. *Phys. Rev. B* **94**, 195410 (2016).
56. Maroulis, G. Hyperpolarizability of H₂O. *J. Chem. Phys.* **94**, 1182–1190 (1991).
57. Mulencko, S. A., Rudenko, V. I., Liakhovetskyi, V. R., Brodin, A. M. & Stefan, A. Large third-order optical nonlinearities in iron oxide thin films synthesized by reactive pulsed laser deposition. *Opt. Mat.* **60**, 123–127 (2016).
58. Hashimoto, T., Yamada, T. K. & Yoko, T. Third-order nonlinear optical properties of sol-gel derived α -Fe₂O₃, γ -Fe₂O₃, and Fe₃O₄ thin films. *J. Appl. Phys.* **80**, 3184–3190 (1996).
59. Ando, M., Kadono, K., Haruta, M., Sakaguchi, T. & Miya, M. Large third-order optical nonlinearities in transition-metal oxides. *Nature* **374**, 625–627 (1995).
60. Chatman, S., Zarzycki, P. & Rosso, K. M. Surface potentials of (001), (012), (113) hematite (alpha-Fe₂O₃) crystal faces in aqueous solution. *Phys. Chem. Chem. Phys.* **15**, 13911–13921 (2013).
61. Wei, F., Urashima, S.-h, Nihonyanagi, S. & Tahara, T. Elucidation of the pH-dependent electric double layer structure at the silica/water interface using heterodyne-detected vibrational sum frequency generation spectroscopy. *J. Am. Chem. Soc.* **145**, 8833–8846 (2023).
62. Nihonyanagi, S., Mondal, J. A., Yamaguchi, S. & Tahara, T. Structure and dynamics of interfacial water structure studied by heterodyne-detected vibrational-sum frequency generation. *Annu. Rev. Phys. Chem.* **64**, 579–603 (2013).
63. Speelman, R., Marker, E. J. & Geiger, F. M. Quantifying stern layer water alignment before and during the oxygen evolution reaction. *Sci. Adv.* **11**, eado8536 (2025).
64. Fumagalli, L. et al. Anomalously low dielectric constant of confined water. *Science* **360**, 1339–1342 (2018).
65. Catalano, J. G. Weak interfacial water ordering on isostructural hematite and corundum (0 0 1) surfaces. *Geochem. Cosmochim. Acta* **75**, 2062–2071 (2011).
66. Wang, R. et al. Sodium halide adsorption and water structure at the α -alumina (0001)/water interface. *J. Phys. Chem. C* **123**, 15618–15628 (2019).
67. Petrenko, V. F. & Whitworth, R. W. *Physics of Ice* (Oxford University Press, 1999).
68. Xu, P., von Rueden, A. D., Schimmenti, R., Mavrikakis, M. & Suntivich, J. Optical method for quantifying the potential of zero charge at the platinum-water electrochemical interface. *Nat. Mater.* **22**, 503–510 (2023).
69. Xu, P., Huang, A. & Suntivich, J. Phase-sensitive second-harmonic generation of electrochemical interfaces. *J. Phys. Chem. Lett.* **11**, 8216–8221 (2020).
70. Lantz, J. M., Baba, R. & Corn, R. M. Optical 2nd-harmonic generation as a probe of electrostatic fields and flat-band potential at single-crystal tio electrodes. *J. Phys. Chem.* **97**, 7392–7395 (1993).
71. Boamah, M. D. et al. Energy conversion via metal nanolayers. *PNAS* **116**, 16210–16215 (2019).
72. Speelman, R. et al. Figshare.com, Fig. 1A–2D. <https://doi.org/10.6084/m9.figshare.28592531.v1>, (2025).

Acknowledgements

This material is based upon work supported by the U.S. Department of Energy, Office of Science, Office of Basic Energy Sciences, Chemical Science, Geosciences and Biosciences Division through a grant to Northwestern University (R.S., E.J.M., and F.M.G.) (DE-SC0023342) and Pacific Northwest National Laboratory (PNNL) (M.B.) (FWP #80307) and the Geosciences program at PNNL (K.M.R.) (FWP #56674). The US National Science Foundation grant CHE-2153191 and the Air Force Office of Scientific Research (FA9550-16-1-0379) are acknowledged for partial funding for the electrochemical cell design and manufacturing and acquisition of the oscillator used in this work.

Author contributions

F.M.G. conceived of the idea. R.S., E.J.M., J.K., M.E., J.Z.B., Y.Z., A.B.F.M., M.D.B., K.M.R., and F.M.G. designed and carried out the experiments, analyzed the data, and wrote the manuscript. M.B., M.E., Y.Z., and K.M.R. assisted with thin film characterization and data analysis. J.K. and A.B.F.M. prepared the thin films, measured steady state optical absorption, and assisted with electrical impedance measurements and data analysis.

Competing interests

The author declares no competing interests.

Additional information

Supplementary information The online version contains supplementary material available at <https://doi.org/10.1038/s41467-025-58842-y>.

Correspondence and requests for materials should be addressed to Franz M. Geiger.

Peer review information *Nature Communications* thanks the anonymous reviewer(s) for their contribution to the peer review of this work. A peer review file is available.

Reprints and permissions information is available at <http://www.nature.com/reprints>

Publisher's note Springer Nature remains neutral with regard to jurisdictional claims in published maps and institutional affiliations.

Open Access This article is licensed under a Creative Commons Attribution-NonCommercial-NoDerivatives 4.0 International License, which permits any non-commercial use, sharing, distribution and reproduction in any medium or format, as long as you give appropriate credit to the original author(s) and the source, provide a link to the Creative Commons licence, and indicate if you modified the licensed material. You do not have permission under this licence to share adapted material derived from this article or parts of it. The images or other third party material in this article are included in the article's Creative Commons licence, unless indicated otherwise in a credit line to the material. If material is not included in the article's Creative Commons licence and your intended use is not permitted by statutory regulation or exceeds the permitted use, you will need to obtain permission directly from the copyright holder. To view a copy of this licence, visit <http://creativecommons.org/licenses/by-nc-nd/4.0/>.

© The Author(s) 2025